ACADEMIC PRESS

Available online at www.sciencedirect.com

SCIENCE DIRECT®

Journal of Sound and Vibration 265 (2003) 43–60

JOURNAL OF SOUND AND VIBRATION

www.elsevier.com/locate/jsvi

A numerical investigation of the noise radiated by a turbulent flow over a cavity

G.B. Ashcroft, K. Takeda*, X. Zhang

School of Engineering Sciences, University of Southampton, Southampton SO17 1BJ, UK

Received 3 September 2001; accepted 1 July 2002

Abstract

The tonal noise radiated by a two-dimensional cavity submerged in a low-speed turbulent flow has been investigated computationally using a hybrid scheme that couples numerical flow computations with an implementation of the Ffowcs Williams–Hawkings equation. The turbulent near field is computed by solving the short-time-averaged, thin-layer approximation of the Navier–Stokes equations, with turbulence modelled by the Wilcox k–ω model. Second order spatial and temporal discretization schemes with fine grids in the immediate region of the cavity and a small time step were used to capture the unsteady flow physics. Along all external boundaries, a buffer zone is implemented to absorb propagating disturbances and prevent spurious numerical reflections. Comparisons with experimental data demonstrate good agreement in both the frequency and amplitude of the oscillations within the cavity. The unsteady characteristics of the cavity flow are discussed, together with the mechanisms for cavity noise generation. The influence of freestream flow velocity and boundary layer thickness on the frequency and amplitude of the oscillations within the cavity and the nature of the noise radiated to the far field are also investigated. Results indicate that both the frequency and amplitude of oscillation are sensitively dependent on the characteristics of the shear layer spanning the mouth of the cavity.

1. Introduction

Cavities or surface cutouts submerged in low-speed turbulent flows are a common source of noise and increased drag in many transport systems. The understanding of cavity flow phenomena is therefore of significant importance, and has received considerable attention ever since the early work of Krishnamurty [1] and Roshko [2]. The bulk of this work has been experimental, as until recently the inherent complexity of such flows has precluded their accurate numerical modelling.

*Corresponding author. Tel.: +44-23-8059-4467; fax: +44-23-8059-3058.
E-mail address: ktakeda@soton.ac.uk (K. Takeda).

0022-460X/03/$ - see front matter
doi:10.1016/S0022-460X(02)01439-6

Theoretical models, however, have been developed, but are largely semi-empirical and sufficient only for the prediction of the possible resonant frequencies. For a given set of conditions none of these are capable of predicting which modes will be present, the amplitude of these modes, or any possible non-linear interactions between modes. Therefore, alongside experimental methods, numerical simulations currently provide the only means of determining the exact nature of a particular cavity flow field for a given set of conditions.

Although the majority of interest in the cavity flow problem has traditionally come from the aerospace industry, cavity noise can also be a major source of automobile aerodynamic noise due to the flow over cavities such as open windows or door seals. The elimination of such noise can offer a commercial advantage and is becoming of increasing strategic importance. Vehicle noise has received considerable attention over recent years, with a significant amount of research being carried out by car manufacturers and other organizations. Much of this work has focused on reducing structure-borne noise, such as vibration from the engine, gear train or the interaction between tyres and the road [3]. This has resulted in improved interior car sound quality and a reduction in the radiated noise levels. Such achievements in the reduction of structure-borne noise have naturally led to an increased awareness of other sources of noise, such as aerodynamic noise. This is now a significant contributor to interior noise levels at high driving speeds. It stems from a variety of sources including the shedding of vortices from antennae, wings and other protrusions, as well as from turbulent boundary layers, turbulent flow separation and natural turbulence in the oncoming air flow [4].

In this work the noise generation mechanisms due to turbulent flow over a generic car door cavity are investigated computationally. A recent review of noise prediction using computational fluid dynamics (CFD) highlighted the feasibility of simulating aerodynamic noise generated by two-dimensional flow using conventional CFD [5]. Providing sufficient care is taken and validation with experimental work is performed, numerical simulations can provide a wealth of information allowing the modes of oscillation and noise generation mechanisms to be identified and understood.

2. Numerical approach

In theory, the sound generated by turbulent fluid motion may be computed directly by solving the compressible, unsteady Navier–Stokes equations. Unfortunately, even at moderate Reynolds numbers this is enormously expensive. Therefore, to study problems at higher Reynolds numbers it is necessary to use much less computationally intensive approaches, such as large eddy simulation (LES) or unsteady Reynolds-averaged Navier–Stokes (URANS) modelling, in which some form of semi-emprical model is employed to represent the influence of the finer scales of turbulence. However, even with the adoption of such approaches, the direct evaluation of the noise heard by an observer in the far field is still prohibitively expensive. To overcome this difficulty, a hybrid approach is adopted in this work. In the immediate region of the cavity and over a portion of the acoustic near field a compressible URANS solver is employed to model the flow physics. The farfield characteristics of the radiated sound field are evaluated using an integral formulation of the acoustic analogy, with the source data provided by the near field numerical simulations.

2.1. Near field

The CFD code CFL3D [6] is employed to model the near field unsteady cavity flow physics. Although CFL3D has not been specifically designed for aeroacoustic problems, it has been shown to be able to resolve flow structures responsible for the noise generation process when suitably fine mesh and time steps are used [7]. CFL3D solves the compressible, three-dimensional, time-dependent, thin-layer Reynolds averaged Navier–Stokes equations on structured grids using a finite volume formulation. For the work undertaken here CFL3D is configured in a 2-D mode. The governing equations written in generalized co-ordinates and conservative form are:

$$\frac{\partial \hat{\mathbf{Q}}}{\partial t} + \frac{\partial(\hat{\mathbf{F}} - \hat{\mathbf{F}}_v)}{\partial \xi} + \frac{\partial(\hat{\mathbf{G}} - \hat{\mathbf{G}}_v)}{\partial \eta} = 0 \tag{1}$$

where

$$\hat{\mathbf{Q}} = \frac{\mathbf{Q}}{J} = \frac{1}{J}\begin{bmatrix} \rho \\ \rho u \\ \rho v \\ e \end{bmatrix}, \tag{2}$$

$$\hat{\mathbf{F}} = \frac{1}{J}\begin{bmatrix} \rho U \\ \rho U u + \xi_x p \\ \rho U v + \xi_y p \\ (e+p)U \end{bmatrix}, \qquad \hat{\mathbf{F}}_v = \frac{1}{J}\begin{bmatrix} 0 \\ \xi_x \tau_{xx} + \xi_y \tau_{xy} \\ \xi_x \tau_{xy} + \xi_y \tau_{yy} \\ \xi_x b_x + \xi_y b_y \end{bmatrix}, \tag{3}$$

$$\hat{\mathbf{G}} = \frac{1}{J}\begin{bmatrix} \rho V \\ \rho V u + \eta_x p \\ \rho V v + \eta_y p \\ (e+p)V \end{bmatrix}, \qquad \hat{\mathbf{G}}_v = \frac{1}{J}\begin{bmatrix} 0 \\ \eta_x \tau_{xx} + \eta_y \tau_{xy} \\ \eta_x \tau_{xy} + \eta_y \tau_{yy} \\ \eta_x b_x + \eta_y b_y \end{bmatrix}. \tag{4}$$

The contravariant velocities are given by

$$\begin{aligned} U &= \xi_x u + \xi_y v, \\ V &= \eta_x u + \eta_y v. \end{aligned} \tag{5}$$

The vector $\mathbf{Q}$ represents density, momentum and total energy per unit volume. The pressure p is related to the conservative flow variables by the equation of state for an ideal gas

$$p = (\gamma - 1)[e - \rho(u^2 + v^2)/2]. \tag{6}$$

The equations are non-dimensionalized with respect to freestream density p_∞, sound speed c_∞, and reference length A, where A equals the length of the cavity opening in the streamwise direction (Fig. 1). The shear stress and heat flux terms are defined in tensor notation (summation convention implied) as

$$\tau_{x_i x_j} = (\mu + \mu_T)\frac{M_\infty}{Re}\left[\left(\frac{\partial u_i}{\partial x_j} + \frac{\partial u_j}{\partial x_i}\right) - \frac{2}{3}\frac{\partial u_k}{\partial x_k}\delta_{ij}\right], \tag{7}$$

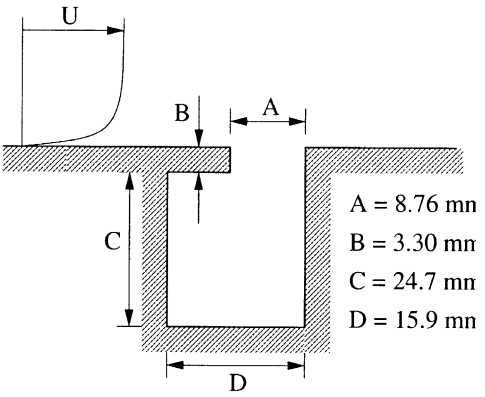

Fig. 1. Cavity geometry.

$$b_{x_i} = u_j \tau_{x_i x_j} - \dot{q}_{x_i}, \qquad \dot{q}_{x_i} = \frac{M_\infty}{Re(\gamma - 1)} \left(\frac{\mu}{Pr} + \frac{\mu_T}{Pr_T} \right) \frac{\partial c^2}{\partial x_i}, \tag{8}$$

where M_∞ is the freestream Mach number, Re is the Reynolds number, μ is the molecular viscosity, μ_T is the turbulent eddy-viscosity (see below), and Pr and Pr_T are the laminar and turbulent Prandtl numbers, respectively. In contrast with typical applications of the thin layer approximation, derivatives are retained in both co-ordinate directions in the shear and heat flux terms. Only those terms originating from cross derivatives are neglected.

The equations are solved implicitly in time using a three-factor approximate factorization scheme. To recover second order temporal accuracy it is necessary to employ a sub-iteration strategy. The *t–TS* [8] option is used here with 10 sub-iterations per physical time step. Fluxes at the cell faces are calculated by the flux-difference splitting method of Roe. Second order accurate upwind-biased spatial differencing is used for the inviscid terms, whilst the viscous derivatives are computed using second order central differencing.

The effects of turbulence on the short-time-averaged flow quantities are simulated through the modelling of the Reynolds stresses which appear in the governing equations as a result of the short-time-averaging procedure. In this work the two-equation Wilcox k–ω model [9] is employed. As with virtually all other two-equation turbulence models this model is based on the Boussinesq eddy-viscosity approximation, and seeks to represent the Reynolds stresses as the product of an eddy-viscosity and the mean strain rate. A detailed description of the Wilcox k–ω model, along with many other turbulence modelling strategies may be found in Ref. [9]. Note that such turbulence models do not describe turbulent fluctuations in detail but provide only the average effects of fluctuations on the short-time averaged flow quantities through the modelling of the Reynolds stress terms.

A particularly important aspect of modelling aeroacoustic phenomena is the need to use non-reflecting boundary conditions along all external boundaries to ensure spurious numerical reflections do not contaminate the solution domain. Many forms of non-reflecting boundary conditions have been proposed, and for problems described in terms of equations linearized about a uniform mean flow, boundary conditions to arbitrary high order of accuracy may be derived

[10]. For non-linear problems the accuracy of such boundary conditions is significantly limited. To overcome this difficulty, the concept of a buffer zone which surrounds the external boundaries of the computational domain has been developed. The nature of such buffer zones vary considerably, and include combinations of grid stretching and filtering, as well as the addition of artificial convection and damping terms to the governing equations. The buffer zone approach is normally combined with traditional stable, low order accurate boundary conditions.

The approach adopted in this study follows the method proposed by Freund [11], in which an artificial damping term is used to drive the solution to a quiescent target state within the buffer region. The artificial damping is added explicitly at the end of every time step in the form of a correction,

$$\mathbf{Q}^{n+1} = \overline{\mathbf{Q}^{n+1}} - \sigma(\overline{\mathbf{Q}^{n+1}} - \mathbf{Q}_{TARGET}), \tag{9}$$

where $\overline{\mathbf{Q}^{n+1}}$ is the solution vector obtained at the end of a time step through the solution of the governing equations. The damping coefficient, σ, varies smoothly from zero at the interface between the buffer zone and the central computational domain to a finite value at the boundary. This is of the form

$$\sigma(\xi) = \varepsilon\left(\frac{L-\xi}{L}\right)^{\beta}, \tag{10}$$

where L is the width of the buffer zone, ξ is the distance from the outer boundary of the buffer zone and ε and β are coefficients which determine the exact nature of the damping coefficient. For the work presented here $\varepsilon = 1$ and the exponent $\beta = 3$. The target data, $\mathbf{Q}_{TARGET}$, represents the local time-averaged flow field in the buffer zone regions. These values are set by computing the steady flow over a flat plate with the same inflow conditions as used in the cavity simulations.

The buffer zone methodology is used in conjunction with the following boundary conditions. To ensure the appropriate upstream turbulent boundary layer profile, the three velocity components u, v and w together with the turbulence quantities, k and ω are prescribed along the inflow boundary of the domain. In accordance with the two-dimensional nature of the simulations the spanwise component of velocity w, is uniformly set to zero. The remaining values are determined using Wilcox's EDDYBL [9] boundary layer program, together with a knowledge of the boundary layer profile just upstream of the cavity. Downstream of the cavity, at the outflow boundary, zeroth order extrapolation is used. Along the upper computational boundary, characteristic 1-D Riemann invariants are solved. All solid walls are modelled with an adiabatic, no-slip boundary condition.

The particular cavity geometry investigated is depicted in Fig. 1. The geometry is representative of an automobile door cavity and comprises a simple rectangular cavity with a small lip or overhang emanating from the upstream face. The basic rectangular structure of the geometry greatly simplifies grid generation and facilitates the use of CFL3D's multi-blocking capacity. The actual computational domain used in the numerical simulations is shown schematically in Fig. 2. To ensure adequate resolution of the upstream turbulent boundary layer and the shear layer developing over the cavity, grid stretching is used to cluster cells along all solid walls and in the region of the shear layer. Along all solid walls $y^+ = O(1)$. Away from the immediate region of the cavity the distribution of the mesh is primarily governed by the need to adequately resolve the acoustic waves.

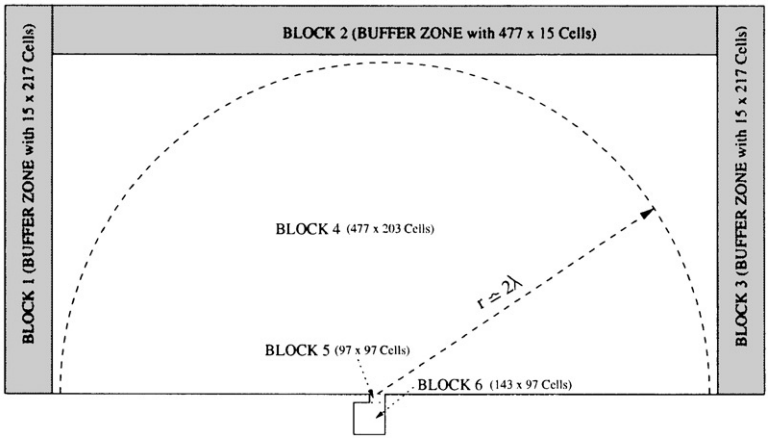

Fig. 2. Computational domain with buffer zones.

The relatively poor resolution characteristics (by which we mean the accuracy with which the scheme represents the exact result over the full range of length scales realizable on a given mesh) of the second order MUSCL scheme employed in CFL3D dictates that a considerable number of cells be employed per wavelength to ensure the accurate propagation of the acoustic waves [12]. Practically, this limits the extent of the computational domain to, at most, a few wavelengths from the source region. The grid contains a total of approximately 130,000 cells distributed between the six blocks comprising the computational domain, as indicated in Fig. 2. Both the grid and time step used have been determined by grid and time step convergence studies, reported earlier by the authors [13].

All simulations begin with the entire flow-field set to freestream values. CFL3D is then initially run in a 'steady state' or non-time accurate mode to obtain a more realistic flow field from which to start time accurate calculations. No form of perturbation or artificial disturbance is imposed on the flow.

2.2. *Far field*

There are several ways in which the farfield characteristics of the sound field may be determined. Conceptually, the most obvious of these is to extend the computational domain to the region of interest and solve the Navier–Stokes equations through out the entire domain. This is, of course, computationally very expensive, and furthermore largely unnecessary, as away from the source region the flow variables generally satisfy a reduced form of the governing equations. A more feasible alternative, therefore, is to patch the source region to a secondary region in which one solves only a simplified version of the governing equations [14]. As this approach still requires that the propagation of the disturbances be computed directly, it is important to use numerical schemes with low dispersion and dissipative error characteristics [15], although, even with the adoption of such schemes, it is still expensive and can be uneconomical to compute the propagation of the disturbances to the true far field, especially when information is required only at a relatively limited number of observer points for evaluating the directivity. An alternative to

these more direct approaches is to employ some form of surface integral method to propagate the pressure disturbances to the far field, such as the Kirchhoff method or the acoustic analogy. In the present study the latter of these approaches is used as it affords a greater degree of flexibility in positioning the integration surface [16].

The particular form of the acoustic analogy used is that due to Ffowcs Williams and Hawkings [17]. This is the most general form of Lighthill's acoustic analogy and is appropriate for computing the acoustic field when solid boundaries play a direct role in the generation of sound. The FW-H equation may be written in differential form as

$$\Box^2(\mathrm{H}p'(\mathbf{x},t)) = \frac{\partial^2}{\partial x_i \partial x_j}(T_{ij}\mathrm{H}) - \frac{\partial}{\partial x_i}\left(L_{ij}\frac{\partial \mathrm{H}}{\partial x_j}\right) + \frac{\partial}{\partial t}\left(\rho_0 U_i \frac{\partial \mathrm{H}}{\partial x_j}\right), \tag{11}$$

where $\Box^2 = (1/c_o^2)\partial^2/\partial t^2 - \partial^2/\partial x_i^2$ is the wave operator, c_o is the ambient speed of sound, t is the observer time, p' is the acoustic pressure, ρ_o is the free-stream density, $\mathrm{H} = \mathrm{H}(f)$ is the Heaviside function, where $f = 0$ defines the integration surface. The terms on the right-hand side of this equation are interpreted as source terms. The first of these is the Lighthill stress tensor T_{ij} and represents the generation of sound by the volume sources. The second term represents the sound generated due to the exertion of unsteady forces by the boundaries on the fluid, and the last term represents the sound generated due to the volume displacement effects of the surface. These last two terms U_i and L_{ij} are defined as

$$U_i = \left(1 - \frac{\rho}{\rho_o}\right)v_i + \frac{\rho u_i}{\rho_o} \tag{12}$$

and

$$L_{ij} = P'_{ij} + \rho u_i(u_j - v_j), \tag{13}$$

respectively. Here ρ is the total density, ρu_i is the momentum in the i direction, v_i is the velocity of the integration surface $f = 0$, and $P'_{ij} = (p - p_o)\delta_{ij} - \sigma_{ij}$ is the compressive stress tensor.

By using a standard Green function approach, Eq. (11) can be written as an integral equation,

$$\begin{aligned} 4\pi \mathrm{H}p'(\mathbf{x},t) = {} & \frac{\partial^2}{\partial x_i \partial x_j}\int_V \left[\frac{T_{ij}}{r|1 - M_r|}\right]_{Ret} \mathrm{d}V \\ & - \frac{\partial}{\partial x_i}\int_S \left[\frac{L_{ij}\hat{n}_j}{r|1 - M_r|}\right]_{Ret} \mathrm{d}S + \frac{\partial}{\partial t}\int_S \left[\frac{U_i \hat{n}_i}{r|1 - M_r|}\right]_{Ret} \mathrm{d}S. \end{aligned} \tag{14}$$

Eq. (14) is not easily employed in computational simulations in its present form, due to the derivatives being taken at the observer time and location. To cast this equation in a more convenient form we follow the approach of Farassat and Succi [18] and the manipulations therein to express the result in terms of source time and location. The resulting form of the equation is known as integral solution 1A, and takes the form

$$p'(\mathbf{x},t) - p'_T(\mathbf{x},t) + p'_L(\mathbf{x},t) + p'_Q(\mathbf{x},t), \tag{15}$$

where

$$4\pi p'_T(\mathbf{x},t) = \int_S \left[\frac{\rho_0(\dot{U}_n + U_{\dot{n}})}{r(1-M_r)^2}\right]_{Ret} \mathrm{d}S + \int_S \left[\frac{\rho_0 U_n(r\dot{M}_r + c_0 M_r - c_o M^2)}{r^2(1-M_r)^3}\right]_{Ret} \mathrm{d}S, \tag{16}$$

$$4\pi p'_L(\mathbf{x},t) = \frac{1}{c_0}\int_S \left[\frac{\dot{L}_r}{r(1-M_r)^2}\right]_{Ret} \mathrm{d}S + \int_S \left[\frac{L_r - L_M}{r^2(1-M_r)^2}\right]_{Ret} \mathrm{d}S + \frac{1}{c_0}\int_S \left[\frac{L_r(r\dot{M}_r + c_0 M_r - c_0 M^2)}{r^2(1-M_r)^3}\right]_{Ret} \mathrm{d}S \tag{17}$$

and $p'_Q(\mathbf{x}, t)$ the term accounting for the quadrupole sources outside the integration surface, may be computed either directly from the volume integral term in Eq. (14) or from any of the appropriate methods available in the literature [19]. However, in the current study this term is neglected. Other than this omission, Eq. (15) is exact and therefore valid in both the near and far field.

In the above equations a dot indicates a time derivative. M_i is the Mach number of the surface in the ith co-ordinate direction, r is the distance from a source point on the surface to the observer, and the subscript r indicates the projection of a vector quantity in the radiation direction. The subscript *Ret* indicates that the integrals are evaluated at each source's retarded time (emission time), given by $\tau = t - |\boldsymbol{x} - \boldsymbol{y}|/c_0$, where $\mathbf{y}$ is the source location, and t and $\mathbf{x}$ are the observer time and position, respectively.

The source terms in the Eqs. (16) and (17) are evaluated using time accurate aerodynamic flow-field data obtained from the CFD calculations. The sound sources are thus given directly in terms of the calculated time-dependent flow field.

3. Results and discussion

Results from numerical simulations of turbulent two-dimensional cavity flows under a range of flow conditions are presented in this Section. The cavity geometry used is that specified as a benchmark problem at the Third Computational Aeroacoustics Workshop [19]. The geometry is representative of a car door cavity and comprises a simple rectangular cavity with a small lip or overhang emanating from the upstream face, as shown schematically in Fig. 1. The neck of the cavity is 8.76 mm wide. The width of the base of the cavity is 15.9 mm and lies 24.7 mm below the cavity lip, which is itself 3.3 mm thick. The length of the cavity in the third dimension is assumed sufficiently large to ensure three-dimensional effects due to cavity ends may be neglected. The freestream Mach number is $M = 0.147$, and the Reynolds number based on the length of the cavity opening is $Re = 29{,}986$. For these freestream flow conditions the incoming boundary layer profile is described by the one-seventh power law, with a boundary layer thickness of 18.44 mm at the mouth of the cavity.

3.1. Cavity flow field

The nature of the flow in the vicinity of the cavity opening may be understood by examining the sequence of instantaneous vorticity contours shown in Fig. 3. These images show the flow in the immediate vicinity of the cavity opening. The images correspond to different times in the oscillation cycle, and highlight the unsteady nature of the shear layer forming as the boundary layer seperates off the lip of the cavity. The oscillations develop as a consequence of shear layer instabilities which amplify small pressure disturbances in a closed feedback loop. The convective growth of these instabilities results in the unsteady impingement of the shear layer on the downstream face of the cavity. As a consequence of this unsteady shear layer behaviour, the pressure in the vicinity of the trailing edge fluctuates in a quasi-periodic manner. This in turn induces an unsteady mass flux in the neck of the cavity.

The growth of the disturbances in the shear layer and the flux of mass into the cavity are shown in the space–time plots of Fig. 4. The first of these, Fig. 4a, shows the flux of mass across the opening into the neck of the cavity. The darker regions indicate a flux of mass into the cavity, whereas the lighter regions represent the expulsion of mass from the cavity. Neglecting the initial starting transients, the periodic nature of the disturbances and their growth with distance downstream of the cavity leading edge is clear. Furthermore, it may be seen that the disturbances in the shear layer follow a linear path in space–time. This implies that the disturbances travel at constant speed across the entire cavity opening. By inspection, the convective velocity of the disturbances normalized by the freestream flow velocity is found to be $U_c = 0.34$. This figure is towards the lower end of the values reported in the literature on cavity flows [20], a fact that may be accounted for by the unusually thick boundary layer relative to the dimensions of the cavity.

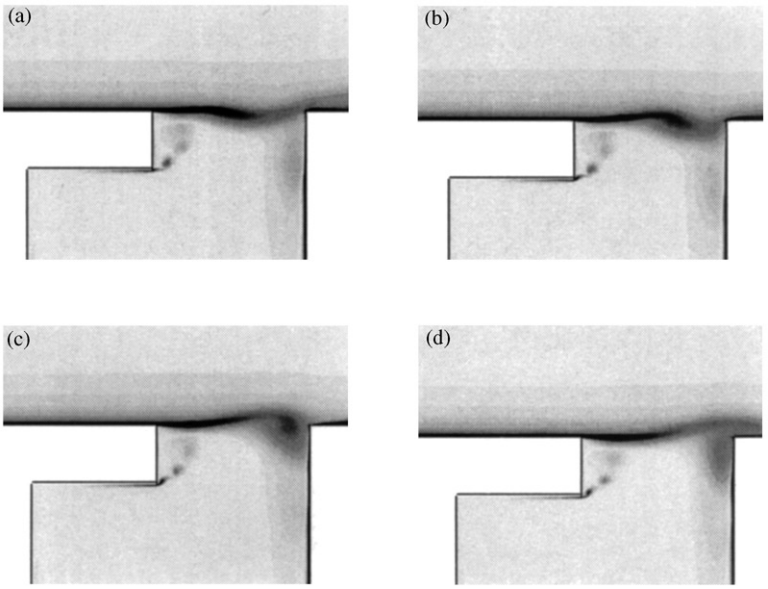

Fig. 3. Instantaneous vorticity contour sequence: (a) $\tau = 0.00$, (b) $\tau = 4.00$, (c) $\tau = 8.00$ and (d) $\tau = 12.00$.

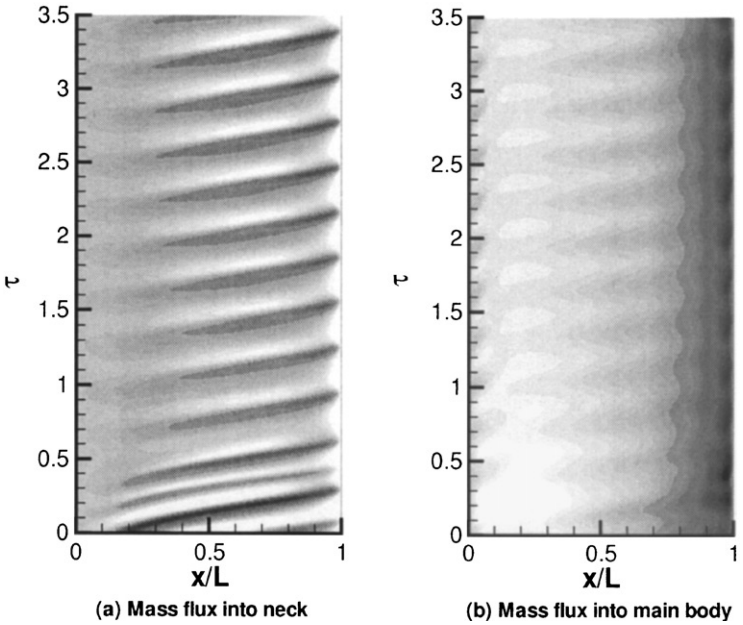

Fig. 4. Mass flux into cavity.

The second of the space–time plots, Fig. 4b, shows the flux of mass from the neck of the cavity to the main body. This shows the inflow of mass is concentrated towards the rear face of the cavity, whereas mass expulsion occurs more evenly over the remainder of the cavity opening. Inspection of the time history of the surface pressures within the main body, however, shows that this concentrated injection of mass gives rise to an essentially uniform change in pressure and density within the cavity.

The cycle of oscillation can be described as follows. As the pressure at the trailing edge increases due to the impingement of the shear layer, a flux of mass into the main body of the cavity results. During this phase the density and pressure increase within the main body of the cavity. As the shear layer continues to evolve with time the pressure in the region of the trailing edge reduces as the shear layer is deflected over the corner. As this occurs mass flows from the cavity and the density and pressure reduce. The feedback loop is closed, as the density and pressure perturbations radiate together as sound from the cavity, perturbing the shear layer. As in the present case, when the frequency of the disturbance is suitably in phase with the developing shear layer, resonance occurs.

The flow within the cavity itself is characterized by a large region of slow recirculating flow, accompanied by regions of secondary recirculation in the corners and at the base of the cavity. As a consequence of this recirculating flow, small-scale vortex shedding from the lower edge of the cavity lip may be observed in the sequence of vorticity contours in Fig. 3.

The favourable coupling between the unsteady shear layer and the acoustic feedback from the cavity causes intense pressure fluctuations within the cavity. Under these resonant conditions sound pressure levels (SPL) of over 130 dB have been observed experimentally. The power spectrum of the computed pressure fluctuations along the upstream wall of the cavity (determined

by reconstruction of the cell-centre data) is shown in Fig. 5, along with the experimental data of Henderson [19]. The computational results show that a strong tonal component at just over 1800 Hz dominates the acoustic spectrum, which is in good agreement with the experimental data. The predicted tonal amplitude also closely matches that reported by Henderson, lying within 3 dB of the amplitude measured experimentally.

The nature of the oscillations observed is characteristic of the classic Helmholtz resonator. In order to test the hypothesis that the cavity geometry was indeed acting as a Helmholtz resonator, the following basic Helmholtz theory was used to estimate the frequency of oscillation:

$$f = \frac{c}{2\pi}\sqrt{\left(\frac{S}{d' V}\right)}, \tag{18}$$

where $d' = d + 2d_e$ is the effective length of the fluid in the neck, including end corrections d_e on either side. S is the opening area, V is the volume of the cavity and c is the speed of sound. The effective length may be estimated in a number of ways, but here Rayleigh's method based on a piston in a baffle [21] is adopted. This is a simple iterative method, and provides an estimate of the resonant frequency to be $f \approx 1850$ Hz, which is in good agreement with the numerical and experimental values. To further assess the accuracy of this basic theory and the validity of the description of the system as a Helmholtz resonator, a number of additional simulations were performed under the same flow conditions, but with modifications to the basic geometry. These results are summarized in Table 1.

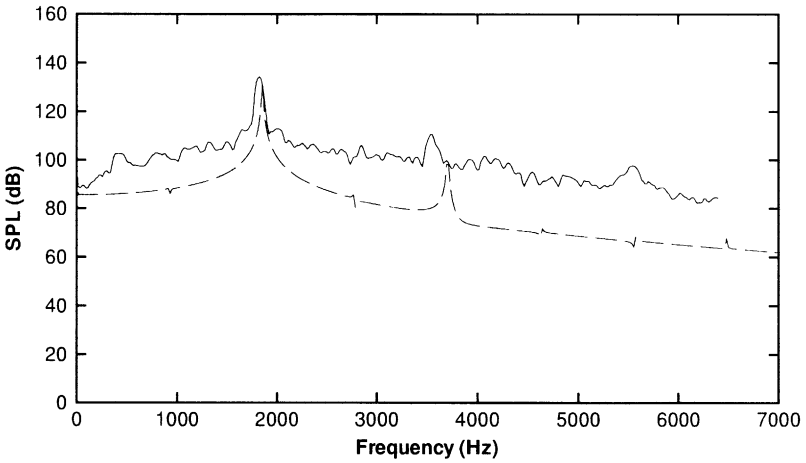

Fig. 5. Cavity wall pressure spectrum:——, experimental and—— –, computational.

Table 1
Influence of geometry on frequency of resonance

Cavity depth (mm)	24.70	30.00	18.00
Computed frequency (Hz)	1820	1740	2000
Estimated frequency (Hz)	1850	1650	2230

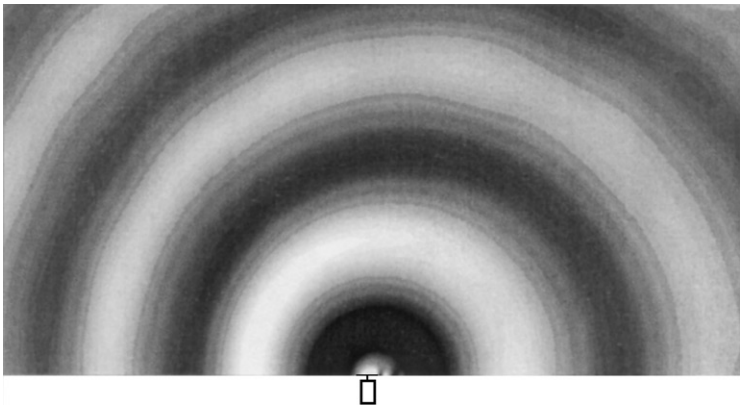

Fig. 6. Instantaneous pressure perturbation contours.

Clearly the general trends are predicted, which would indicate the essential mode of oscillation is that of a Helmholtz resonator; however, the accuracy of the estimated frequency varies considerably and demonstrates the estimate given for the base line geometry was quite fortuitous. This basic theory can therefore be used to provide a guide to the effects of geometry change, but to determine the precise values it is necessary to employ more sophisticated modelling techniques.

The sound field in the immediate region of the cavity has been computed directly in the simulations by extending the computational domain a distance of approximately 2λ from the mouth of the cavity, were λ is the wavelength of the fundamental frequency. A snapshot of the sound field in this region is shown in Fig. 6. The convection of the sound field by the mean flow is apparent. On closer inspection the Doppler shift induced by the low-speed mean flow may also be discerned through examination of the wavelengths of the disturbances propagating away from the cavity region.

3.2. *Acoustic far field*

The farfield characteristics of the radiated sound field are evaluated using the Ffowcs Williams–Hawkings integral equation. The application of this method requires the definition of an integration surface. Numerically, the size and position of this surface can have an influence on the accuracy of the predictions. In the current study the surface runs parallel with the outer wall of the cavity, and extends a finite distance in the spanwise direction. To provide data for the entire surface the two-dimensional CFD data is replicated in the spanwise direction. In doing so the flow is assumed to perfectly coherent over this length. It has been demonstrated by Brentner et al. [22] that when the length over which the surface extends corresponds approximately to the length over which the flow is coherent, accurate estimates of the sound pressure levels may be obtained. Unfortunately, this information is not available for the particular geometry and set of flow conditions considered here. However, as in the current computational work the extent of the computational domain is such that a portion of the acoustic near field is computed directly, the replication length may be established by using the FW-H code to evaluate the sound field in this same region. In this way the replication length may be calibrated so that the two solutions match

well. Using this approach a replication length of approximately $18A$ (where A is the size of the cavity opening) was found to be most accurate.

The length of the integration surface in the streamwise direction is also an important factor. Ideally, the surface would be of infinite extent, however, in practice the surface must be truncated. In the current study the streamwise extent of the surface is limited by the size of the computational domain. It is therefore important to assess the convergence of the integrals over the limited surface that may be used. The computed pressure history for an observer located 2 m directly above the mouth of the cavity is shown in Fig. 7 for a range of surfaces of varying streamwise length. As the length of the integration surface is increased the difference between successive surfaces decreases, with the final two pressure traces being virtually indistinguishable at this scale.

The farfield directivity of the radiated noise is evaluated by computing the pressure signals at several observers points, located on an arc of radius 2 m, focused about the centre of the cavity opening. The computed directivity of dominant fundamental frequency is shown in Fig. 8. The sound is found to radiate almost uniformly in all directions, although the radiation is observed to be slightly stronger in the upstream direction. The amplitude in the upstream arc is approximately 0.5 dB greater than in the downstream arc, with an amplitude of 93 dB.

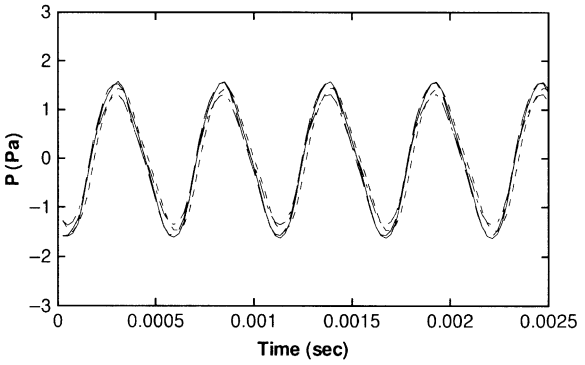

Fig. 7. Pressure time histories for different integration surfaces:— — —, IS length = 90 A; — — —, IS length = 85 A; ——, IS length = 80 A; and — · — · —, IS length = 70 A.

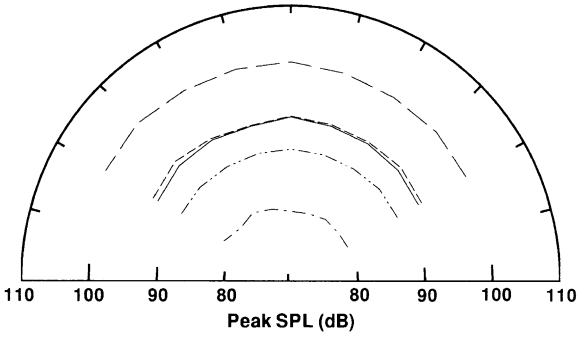

Fig. 8. Farfield directivity pattern for dominant frequency: — —, $U_\infty = 50$ m/s, $\delta = 18.44$ mm; — — —, $U_\infty = 55$ m/s, $\delta = 18.12$ mm; —·—· –, $U_\infty = 45$ m/s, $\delta = 18.67$ mm; —— $U_\infty = 50$ m/s, $\delta = 7.23$ mm; and —· ·—· ·—· · –, $U_\infty = 50$ m/s, $\delta = 3.93$ mm.

3.3. Effects of freestream velocity

In order to assess the influence of freestream flow velocity on the nature of the cavity oscillations and the radiated noise, additional simulations have been performed. Two freestream flow speeds have been considered, $U_\infty = 45$ m/s and $U_\infty = 55$ m/s. The inflow conditions for these cases were chosen to ensure the thickness of the boundary layers at the lip of the cavity were close to the original case, in which $\delta \approx 19$ mm.

At these flow speeds the mechanism of oscillation is found to be unchanged. However, the frequency and amplitude of the oscillations are different in both cases from the those observed at 50 m/s. This is most clearly seen in the spectra of the fluctuating wall pressure measured on the upstream face of the cavity (Fig. 9). When examining these spectra it should be noted we are concerned only with the tonal components, and the broadband features of the signals are beyond the scope of the current approach. Examination of these figures show that both the amplitude and frequency increase with flow speed. At a flow speed of 45 m/s the fundamental frequency of oscillation is approximately 1700 Hz and the amplitude of the oscillation is slightly below 120 dB. As the flow speed is increased by just 10–55 m/s, the amplitude of oscillation increases substantially to over 139 dB, and the frequency increases to 1960 Hz.

The farfield characteristics of the radiated noise are shown in Fig. 8. Clearly at the higher speed of 55 m/s, significantly more noise is radiated to the far field from the cavity. The radiated noise is also found to be more directional, with the amplitude in the upstream arc almost 2 dB larger than that downstream. This trend is consistent with basic theory for point sources in motion, and would therefore suggest the enhanced directivity observed at the higher flow speed is principally a result of the increased source velocity. The largest farfield amplitude is found to occur at approximately 135°, where the angle is measured counter clockwise from the downstream edge. However, the amplitude at this angle is only marginally higher than those surrounding it. At the lower speed, the level of radiated noise falls significantly below the levels observed at the higher speeds, to 80 dB in the downstream direction and just over 81 dB in the upstream direction.

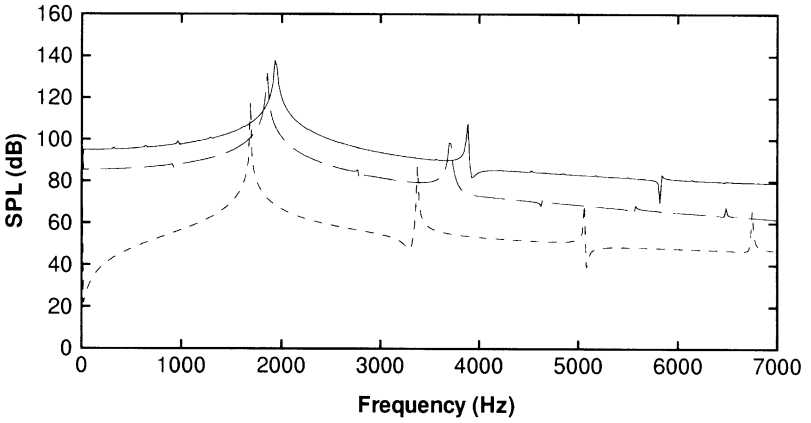

Fig. 9. Influence of freestream flow speed on cavity wall pressure: ———, $U_\infty = 55$ m/s; — — — — $U_\infty = 50$ m/s; and ——, $U_\infty = 45$ m/s.

3.4. Effects of boundary layer thickness

In order to study the effects of incoming boundary layer thickness on the nature of the induced cavity oscillations, two further simulations were performed. In both cases the basic flow parameters remain unchanged, with the same Reynolds number and Mach number. The thinner boundary layers are achieved by specifying a freestream condition on the inflow boundary. Boundary layer thickness is then determined by the extent of the solid wall upstream of the cavity. In the case of the thinnest boundary layer, the solid wall does not extend the entire way to the inflow boundary. In this case a symmetry condition is employed over the remaining region. The integral properties of the boundary layers 5 mm upstream of the cavity leading edge are given in Table 2.

Examination of the instantaneous vorticity contours for the two thinner boundary layer cases, reveals that the flow fields exhibit the same characteristics as the thicker boundary layer flow, with the processes of shear layer impingement and unsteady mass flux dominating the flow in the mouth of the cavity. However, when the fluctuating cavity wall pressures are plotted and compared it is clear that the nature of the upstream boundary layer does indeed have a significant effect on the both the amplitude and frequency of the cavity pressure oscillations. This is shown in the pressure time history plots in Fig. 10. It is found that as boundary layer thickness increases, the tonal frequency decreases from a value of approximately 2070 Hz when $\delta = 3.93$ mm to a value of 1820 Hz when $\delta = 18.44$ mm. The amplitude, however, is found to be largest at the intermediate

Table 2
Cavity flow boundary layer data

U_∞ (m/s)	δ (mm)	δ^* (mm)	θ (mm)	H
50	18.44	2.15	1.71	1.26
50	7.23	1.00	0.77	1.30
50	3.93	0.54	0.40	1.35

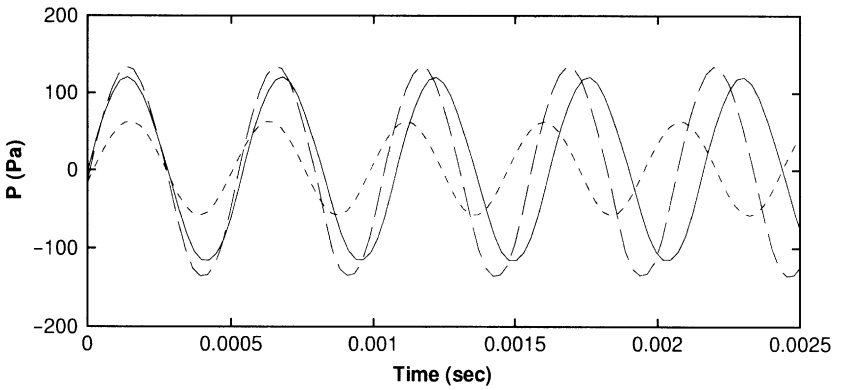

Fig. 10. Cavity wall perturbation pressure time histories: ———, $\delta = 18.44$ mm; — — — —, $\delta = 7.23$ mm; and ——, $\delta = 3.93$ mm.

boundary layer thickness. This suggests that the stability characteristics of the mean flow profile play an important role in determining the amplitude and also the frequency of the oscillations. Examination of the shear layer development across the mouth of the cavity reveals that the disturbances convect at slightly higher speeds in the thinner boundary layers, which accounts for the increases in frequency of oscillation with reduced boundary layer thickness. The growth of the disturbances, however, is found to vary with boundary layer thickness. In the case of the thinnest boundary layer the least growth is observed. This has the result of weakening the oscillatory motion of the shear layer in the region of the cavity trailing edge, and thus the strength of the forcing which drives the cavity resonance.

The impact of these factors on the characteristics of the noise radiated to the far field is shown in Fig. 8. Clearly, the trends in amplitude follow those observed in the oscillations within the cavity. The boundary layer of thickness $\delta = 3.93$ mm exhibits the weakest radiation of the three cases, with an amplitude of approximately 89 dB in the upstream direction and 88 dB in the downstream direction. The strongest radiation is observed for $\delta = 7.23$ mm case. Here the amplitude of the radiation in the upstream direction is almost 94 dB and that in the downstream arc approximately 93 dB. In both cases the directivity is similar to that observed in all cases, with marginally stronger radiation in the upstream direction.

4. Conclusions

A hybrid approach combining a compressible unsteady RANS flow solver with an integral formulation of the acoustic analogy has been employed to investigate the unsteady flow and resulting acoustic radiation from a cavity geometry submerged in a low-speed turbulent flow. Through validation against experimental data this approach has been shown capable of capturing the tonal components of the noise spectrum.

For the set of flow conditions considered, the flow in the mouth of the cavity is found to be dominated by the time-dependent behaviour of the shear layer, and the unsteady flux of mass into and out of the main body of the cavity. The flow within the cavity itself is still, however, largely quiescent and characterized by a large region of slowly recirculating flow. As a consequence of this motion, small-scale vortex shedding off the lower edge of the cavity lip is observed. The unsteady flux of mass in the neck of the cavity causes the pressure and density to fluctuate within the cavity body. At the flow speeds considered in this work a favourable coupling develops between the undulating shear layer and the cavity oscillations, such that a condition of resonance occurs. Under these conditions, large-amplitude fluctuations in pressure and density are observed within the cavity, which give rise to significant levels of noise radiation.

The influence of the freestream flow speed and the nature of the upstream boundary layer is found to be varied. Increasing freestream flow speed significantly increases the amplitude of the noise radiated, and to a lesser degree the frequency of oscillation. The directivity of the radiated sound field is also found to increase marginally with flow speed, in a manner that leads to an increase in the noise radiated in the upstream direction. The properties of the upstream boundary layer are also found to be important in determining both the amplitude and frequency of the oscillations. For the present set of flow conditions it is found that as boundary layer thickness is reduced, the frequency of oscillation increases. This is believed to be due to the higher convective

speeds of the disturbances in the shear layer observed in the thinner boundary layers. The amplitude of oscillation is found to initially increase with boundary layer thickness and decrease as the value is further increased. All of these factors point to the sensitive dependence of the oscillations on the stability characteristics of the shear layer spanning the mouth of the cavity.

Acknowledgements

The authors would like to thank Dr. Christopher Rumsey for the CFL3D code, Dr. Brenda Henderson for providing the experimental data, and Professors Geoffrey Lilley and Christopher Morfey for many useful suggestions. Additionally, the first author wishes to thank the EPSRC for providing a Ph.D. studentship.

References

[1] K. Krishnamurty, Acoustic radiation from two-dimensional rectangular cutouts in aerodynamic surfaces, NASA TN 3487, 1955.
[2] A. Roshko, Some measurements of flow in a rectangular cutout, NASA TN 3488, 1955.
[3] Vehicle noise and vibration, Institute of Mechanical Engineers Conference Transactions, ISBN 1-86058-145–5.
[4] N. Lida, Measurement and evaluation of aerodynamic noise, Society of Automobile Engineers Paper 1999-01-1124, 1999.
[5] S. Ogawa, T. Kamioka, Review of aerodynamic noise prediction using CFD, 1999 Society of Automobile Engineers Paper 1999-01-1126, 1999.
[6] S.L. Krist, R.T. Biedron, C.L. Rumsey, CFL3D User's Manual (Version 5.0), NASA TM 1998–208444, 1998.
[7] B.A. Singer, D.P. Lockard, K.S. Brentner, M.R. Khorrami, M.E. Berkman, M. Choudhari, Computational acoustic analysis of slat trailing-edge flow, American Institute of Aeronautics and Astronautics Paper 1999–0231, 1999.
[8] C.L. Rumsey, M.D. Sanetrik, R.T. Biedron, N.D. Melson, E.B. Parlette, Efficiency and accuracy of time-accurate turbulent navier–Stokes Computations, American Institute of Aeronautics and Astronautics Paper 1995–1835, 1995.
[9] D.C. Wilcox, Turbulence Modeling for CFD, Ist edition, DCW Industries, Inc, USA, 1993.
[10] W.C. Rowley, T. Colonius, Numerically nonreflecting boundary conditions for multidimensional Aeroacoustic Computations, American Institute of Aeronautics and Astronautics Paper 1998–2220, 1998.
[11] J.B. Freund, Proposed inflow/outflow boundary conditions for direct computation of aerodynamic sound, American Institute of Aeronautics and Astronautics Journal 35 (1997) 740–742.
[12] D.V. Nance, K. Viswanathan, L.N. Sankak, Low-dispersion finite volume scheme for aeroacoustic applications, American Institute of Aeronautics and Astronautics Journal 25 (1997) 255–262.
[13] G.B. Ashcroft, K. Takeda, X. Zhang, in: Proceedings of Seventh International Congress on Sound and Vibration, 2000. Computational modeling of the aeroacoustics of a door cavity flow oscillation,
[14] J.B. Freund, K.S. Lele, P. Moin, Matching of near/far-field equation sets for direct computation of aerodynamic sound American Institute of Aeronautics and Astronautics Paper 1993–4326, 1993.
[15] C.K.W. Tam, J. Webb, Dispersion-relation-preserving finite difference schemes for computational acoustics, Journal of Computational Physics 107 (1993) 262–281.
[16] B.A. Singer, K.S. Brentner, D.P. Lockard, G.M. Lilley, Simulations of acoustic scattering from a trailing edge, American Institute of Aeronautics and Astronautics Paper 1999–0231, 1999.
[17] J.E. Ffowcs Williams, D.L. Hawkings, Sound generation by turbulence and surfaces in arbitrary motion, Philosophical Transactions of The Royal Society 246 (1969) 321–342.
[18] F. Farassat, G.P. Succi, The prediction of helicopter discrete frequency noise, Vertica 7 (1983) 309–320.

[19] B. Henderson, Automobile noise involving feedback, Proceedings of Third Computational Aeroacoustics Workshop on Benchmark Problems, 1999.
[20] J.E. Rossiter, Wind-Tunnel experiments on the flow over rectangular cavities at subsonic and transonic speeds, Aeronautical Research Council Reports and Memoranda No. 3438, 1966.
[21] L. Rayleigh, Theory of Sound, 2 Vol, 2nd Edition Dover Publications, New York 1945 re-issue, 1877.
[22] K.S. Brentner, J.S. Cox, C.L. Rumsey, B.A. Younis, Proceedings of the Second Computational Aeroacoustics Workshop on Benchmark Problems, 1997. Computational of sound generated by flow over a cylinder: an acoustic analogy approach.